Computational Particle Mechanics (2024) 11:2089–2104
https://doi.org/10.1007/s40571-024-00753-8

Qualitative and quantitative analyses of particulate flows in rotating drums using a DEM-based approach

Luis Angeles[1] · **Kennia Velez**[1] · **Cesar Celis**[1]

Received: 1 September 2023 / Revised: 9 February 2024 / Accepted: 11 March 2024 / Published online: 29 April 2024
© The Author(s) under exclusive licence to OWZ 2024

Abstract

In mineral processing, ore grinding is an energy-intensive process. Tumbling mills used in grinding processes can be accounted for as rotating drums with liners. As part of an effort to evaluate ways of reducing energy consumption in such systems, therefore, particulate flows in rotating drums are studied in this work. More specifically, using a new DEM tool, which is one of the modules of a larger in-house computational package called CFLOWSS, particulate flows in rotating drums are qualitatively and quantitatively analyzed. The results from such analyses are compared with experimental ones and other numerical results obtained using a commercial DEM software. In qualitative terms, the CFLOWSS results show a relatively good agreement with experimental photographs previously taken in a laboratory. In quantitative terms, in turn, the CFLOWSS predictions show a strong correspondence with those ones made by the commercial software. For instance, the relative discrepancies of the boxplots' medians associated with the number of contacts, power, and forces predicted by both (in-house and commercial) tools present values smaller than 8%. At a 60 RPM drum rotation velocity, indeed, the number of contacts related discrepancies reach values as low as 0.8%. Some of the contributions of this work involve (i) the development of a new DEM tool capable of realistically describing particulate flows in rotating drums, and (ii) the use of statistical treatments to quantitatively analyze DEM results. This last aspect is important because this sort of assessments provides an improved way to analyze the behavior of particulate flows.

Keywords Rotating drums · Particulate flows · Quantitative analyses · DEM · CFLOWSS

1 Introduction

In mineral processing, comminution involving the release of the valuable mineral from the rock is a key process. This process usually includes three stages, blasting, crushing, and grinding [1]. Comminution processes, especially the grinding ones, are the major energy consumers in mines [2]. For instance, it has been reported [3] in the past that, in a particular copper mine, comminution consumes 36% of total energy, the grinding stage being the largest energy consumer. In the same report, it was found that the energy consumption associated with comminution represents about 25% of the total energy consumed in the mine site, being thus the single biggest energy user. Indeed, comminution processes may use around 2% of the total electrical energy generated globally [2], or 1% of total final energy consumed globally [3]. Additionally, the wear of liners and grinding media (balls or bars) also generate indirect energy consumption, which is not generally reported by mining companies. This indirect energy consumption can be between 30 and 50% of the direct one [4].

Particulate flows (two-phase, liquid–solid flows), known as slurries, are common in both industry and nature. In the mining industry, the transport and grinding of mineral-slurries involve complex processes whose behavior is difficult to evaluate experimentally. Numerical models based on computational fluid dynamics (CFD) allow both studying these complex processes in depth and having a better understanding of the associated phenomena. There are two general approaches for modeling particulate flows, (i) Eulerian–Eulerian and (ii) Eulerian–Lagrangian. The particulate phase present in such flows can be modeled in turn using a continuous approach or a discrete one [5]. Continuous approaches involve modeling a large number of discrete particles as an

✉ Luis Angeles
langelesr@pucp.edu.pe

[1] Mechanical Engineering Section, Pontificia Universidad Católica del Perú, Av. Universitaria 1801, San Miguel, Lima 32, Lima, Peru

artificial continuous medium. This approach is well known as the Eulerian–Eulerian one, where both fluid and particulate flows are modeled using Eulerian approaches. The main disadvantage of continuous approaches is that the local behavior of individual particles is not accounted for. In contrast, discrete approaches describe the motion and contact of each discrete particle individually. Compared to the continuous ones, the main disadvantage of discrete approaches relates to their relatively high computational cost. The best-known method belonging to the category of discrete approaches is the one based on discrete elements (DEM). DEM-based approaches represent indeed Lagrangian methods.

Particulate flows featuring high particle concentrations, such that particle–particle interactions dominate the mechanics, are called granular flows [6]. Granular flows are found indeed in nature and in many manufacturing and industrial applications (almost 50% of products are granular or involves the use of granular material) [7, 8]. For instance, mineral grinding is performed in rotating cylindrical vessels called tumbling mills. In these mills, physical phenomena like compression, chipping, and abrasion occur between the granular material and the grinding media in a wet or dry environment (wet/dry grinding). Tumbling mills usually have liners that help both moving the mineral being ground and avoiding its segregation. To study the complex physical processes occurring inside tumbling mills, simplified models are usually first developed. A relatively simple model describing the rotation of discrete particles inside a cylindrical vessel without liners is a rotating drum. These drums are used in mixing, segregation, heating, drying, and chemical reactions related applications in the metallurgical, food, pharmaceutical, and chemical industries [7, 9].

According to their rotational speed, filling degree, and wall friction coefficient, rotating drums feature different flow regimes, sliding, slumping (or avalanching), rolling, cascading, cataracting, and centrifuging [10]. As expected, the physical phenomena occurring inside tumbling mills are mostly related to particle motion inside them. Particularly, there are two types of particle motion inside a tumbling mill, (i) cataracting and (ii) cascading [11]. Cataracting is related to the motion of particles following approximately a parabolic trajectory and impacting against the mill toe. Cascading in turn is characterized by sliding and rolling downward on the material surface. This flow regime can also be considered as a rolling one with intense particle motion. Notice that the referred particle motion produces many contacts between grinding media, minerals, and the tumbling surfaces responsible for the different comminution mechanisms (impact, chipping, and abrasion) within the tumbling mill. Because the interest in this work is on mining-related applications, the focus here will be on the rolling, cascading, and cataracting flow regimes.

For modeling the dynamics of dry granular flows, there are two main DEM-based approaches, (i) the discrete element method via penalty (DEM-P), and (ii) the discrete element method via complementarity (DEM-C) [12, 13]. First, the DEM-P approach is the classical one based on the work of Cundall [14] and used in soft matter physics and geomechanics. It is a regularization (smoothing) method that uses a relaxation of the rigid-body assumption [13, 15]. Thus, this approach assumes that the bodies deform slightly, and there is an interpenetration at the contact point [12, 13, 15]. During a contact, at each time step, a surrogate deformation of the two bodies in contact is produced based on their interpenetration values and shapes. This scheme uses explicit time integrators to solve Newton's and Euler's second laws of motion for individual particles. The DEM-C approach, in turn, is based on the works of Moreau [16] and Jean [17] and is used in robotics and computer graphics applications. DEM-C considers the bodies completely rigid and enforces non penetration through complementary conditions [13]. As such, this approach uses non-differentiable steep contact laws and uses implicit methods for solving in time [15]. DEM-P and DEM-C have fundamental differences in the way they model the dynamics of dry granular flows. Even though both methods predict the macroscale flow behavior based on the dynamics of the microscale one, each approach has advantages over the other for specific problems. For instance, when modeling many monodisperse particles in flow configurations featuring high internal stresses, DEM-P is faster and more suitable to capture the related macroscale and microscale responses than DEM-C [13]. DEM-C is designed to use relatively large time steps but, in flow configurations involving a large number of particles, the granular dynamics is characterized by relatively small spatial and temporal scales. Thus, DEM-C loses its advantages in these cases, whereas DEM-P is well suited for them. As tumbling mills and rotating drums involve relatively high stresses (cataracting regimen, grinding application) and high numbers of discrete particles, the DEM-P approach is used in this work. Notice however that, for the sake of brevity, DEM-P will be simply referred to as DEM.

DEM-based tools are useful for designing and analyzing particulate flows present in several practical applications. Although the discussion of all DEM existing tools is out of the scope of this work, for the sake of argument, it is worth highlighting some of them here. For instance, EDEM [18] is a commercial parallel DEM software that utilizes high-performance computing capabilities to simulate large-scale systems. This software has been designed to take advantage of the processing power of modern CPUs and GPUs, which allows it to simulate complex particle systems more effectively. Similarly, Rocky DEM [19] is a commercial parallel software used in industrial applications such as agriculture, pharmaceutics, and mining, which has been also optimized for high-performance computing. In addition, LIGGGHTS

[5] is an open-source DEM tool that offers a range of features such as parallel processing (MPI and OpenMP), scripting interface, and visualization tools for analyzing simulation results. In most of these tools, the use of physical models other than those already available in them is not an easy task. Besides, coupling these DEM tools to others based on modeling approaches such finite volumes, finite elements, spectral methods, and smooth particle hydrodynamics is even more difficult. In this sense, having a DEM-based tool flexible enough to both try different physical models and couple it to any other modeling approach is desirable and constitutes one of the motivations for this work.

In this work, particulate flows in rotating drums are qualitatively and quantitatively analyzed using a new DEM tool. This new DEM tool constitutes one of the modules of a larger in-house computational package under development called CFLOWSS (Complex FLOWS Solver) [20–23], which aims to numerically solve different complex flows including mineral-slurries. More specifically, this works describes the extension of the CFLOWSS DEM module initially presented in [20] accounting for contact force models, tangential deformation, and 3D particles. Once developed, the new CFLOWSS DEM module is used to analyze particulate flows in rotating drums. Notice that new DEM code is similar to existing commercial tools like EDEM [18] and Rocky DEM [19], but the former allows the implementation of any physical model and its coupling with the other CFLOWSS modules based on different modeling approaches is straightforward. This flexibility constitutes one of the main features of the new DEM tool under discussion here.

The results from such analyses are qualitatively and quantitatively compared with experimental ones and other numerical results obtained using a commercial DEM software [24]. Accordingly, the mathematical model used in the CFLOWSS DEM module is described in Sect. 2. Next, in Sect. 3, the DEM module computational implementation is discussed. The main results obtained in this work, in qualitative and quantitative terms, are presented and discussed in Sect. 4. Finally, the main conclusions drawn from the work carried out here are summarized in Sect. 5. One of the contributions of this work involves the development of a new DEM tool capable of realistically describing particulate flows in rotating drums. Another contribution of this work is the quantitative comparison between the numerical results produced with the new DEM tool and those ones obtained using the commercial DEM software. This last aspect is important because most previous works on this subject only carry out qualitative comparisons of the obtained results.

2 Mathematical model

The mathematical model utilized in the CFLOWSS DEM module developed and utilized here is described in this section. A particular emphasis is put on the particulate flow governing equations, the models used to compute the normal and tangential forces, the tangential contact displacement correction methods, and the explicit timestep solver.

2.1 Governing equations

DEM via penalty [14] is also called the soft sphere approach or the penalty method. As highlighted in Sect. 1, the DEM-P (henceforth DEM) models a granular problem using a collection of deformable elements having simple shapes, mostly spherical ones. Granular material dynamics is governed by Newton's second law of motion and Euler's second law of angular motion respect to the center of mass of each particle. Accordingly, considering a computational domain including N spherical particles, the associated governing equations read as follows [25],

$$m_i \frac{\mathrm{d}\overline{v}_i}{\mathrm{d}t} = m_i \frac{\mathrm{d}^2\overline{x}_i}{\mathrm{d}t^2} = \overline{f}_i\left(\overline{x}_j, \overline{v}_j, \overline{\varphi}_j, \overline{\omega}_j\right), \tag{1}$$

$$I_i \frac{\mathrm{d}\overline{\omega}_i}{\mathrm{d}t} = I_i \frac{\mathrm{d}^2\overline{\varphi}_i}{\mathrm{d}t^2} = \overline{M}_i\left(\overline{x}_j, \overline{v}_j, \overline{\varphi}_j, \overline{\omega}_j\right),\ j = 1, \ldots, N, \tag{2}$$

where $\overline{f}_i$ and $\overline{M}_i$ are, respectively, the sum of forces and torques acting on particle i, and $\overline{x}_i$ and $\overline{v}_i$ represent the position and translational velocity of the particle center, respectively. In turn, $\overline{\varphi}_i$ and $\overline{\omega}_i$ stand for, respectively, the particle angular position and rotational velocity, m_i is the particle mass, and I_i the tensorial moment of inertia. Finally, the subscript j appearing in these equations represents particles other than i that are in contact with particle i.

Notice that when two soft spheres are in contact, the overlap δ_n between them can be computed using suitable particle contact algorithms. With this overlap, and accounting for several constitutive laws based on particle local deformation, particles velocities, and particles material properties [14, 26–31], the normal $\left(\overline{f}_{ij}^{n}\right)$ and tangential $\left(\overline{f}_{ij}^{t}\right)$ force vectors relative to the particles' contact plane are determined.

2.2 Normal force models

The models for the normal and tangential forces used in the CFLOWSS DEM module are mainly based on those ones

Table 1 Normal force models included in the CFLOWSS DEM module

Normal force model	k_{el}^n	k_{diss}^n
Linear spring dashpot model (LSD) [14]	k_n	η_n
Kuwabara and Kono (KKn) [26]	k_{Hertz}	$\eta_n \delta_n^{1/2}$
Tsuji, Tanaka and Ishida (TTIn) [27]	k_{Hertz}	$\eta_n \delta_n^{1/4}$
Zheng, Zhu, and Yu (ZZYn) [28]	k_{Hertz}	$C_n \eta_n (R_{\text{eff}} \delta_n)^{1/2}$

discussed in the work by Norouzi et al. [32]. Therefore, first, the normal force $\overline{f}_{ij}^n$ includes two components, (i) the elastic $\overline{f}_{\text{el}}^n$ and (ii) the dissipative or viscous $\overline{f}_{\text{diss}}^n$ ones. Accordingly, for a linear viscoelastic model, the normal force is defined as,

$$\begin{aligned}\overline{f}_{ij}^n &= \overline{f}_{\text{el}}^n + \overline{f}_{\text{diss}}^n = -f_{\text{el}}^n \overline{n}_{ij} - f_{\text{diss}}^n \overline{n}_{ij} \\ &= -k_{\text{el}}^n \delta_n \overline{n}_{ij} - k_{\text{diss}}^n v_{rn} \overline{n}_{ij},\end{aligned} \tag{3}$$

and for a nonlinear viscoelastic one (Hertzian models) as,

$$\begin{aligned}\overline{f}_{ij}^n &= \overline{f}_{\text{el}}^n + \overline{f}_{\text{diss}}^n = -f_{\text{el}}^n \overline{n}_{ij} - f_{\text{diss}}^n \overline{n}_{ij} \\ &= -k_{\text{el}}^n \delta_n^{3/2} \overline{n}_{ij} - k_{\text{diss}}^n v_{rn} \overline{n}_{ij},\end{aligned} \tag{4}$$

where k_{el}^n is the normal spring stiffness coefficient, k_{diss}^n is the normal damping one, and $\overline{n}_{ij}$ is the normal vector defined as $\overline{n}_{ij} = \frac{\overline{\text{x}}_{\text{j}} - \overline{\text{x}}_i}{\overline{\text{x}}_{\text{j}} - \overline{\text{x}}_i}$. In the nonlinear models used in the DEM module developed here, the normal spring stiffness is calculated using the Hertz theory k_{Hertz}. In turn, as highlighted in Table 1, which summarizes the normal force models implemented and currently available in the CFLOWSS DEM module, the normal damping coefficient is given by different models.

It is worth noticing here that k_{Hertz} is calculated as $\frac{4}{3} E_{\text{eff}} \sqrt{R_{\text{eff}}}$, with R_{eff} being the effective radius and E_{eff} the effective Young's modulus, and η_n is the damping coefficient associated with a specific model. C_n is in turn a correction factor of viscous force associated with the ZZYn model [28]. Here, η_n is calculated using material properties.

2.3 Tangential forces models

Second, in a similar fashion to the normal force, the estimated tangential force $\left(\overline{f}_o^t\right)$ includes two components, (i) the elastic $\left(\overline{f}_{\text{el}}^t\right)$ and the dissipative or viscous $\left(\overline{f}_{\text{diss}}^t\right)$ ones. Then, for a linear or nonlinear viscoelastic model, the estimated tangential force is defined as,

$$\begin{aligned}\overline{f}_o^t &= \overline{f}_{\text{el}}^t + \overline{f}_{\text{diss}}^t = -f_{\text{el}}^t \overline{t}_{ij} - f_{\text{diss}}^t \overline{t}_{ij} \\ &= -k_{\text{el}}^t \delta_t \overline{t}_{ij} - k_{\text{diss}}^t v_{rt} \overline{t}_{ij} = -k_{\text{el}}^t \overline{\delta}_t - k_{\text{diss}}^t \overline{v}_{ij}^t,\end{aligned} \tag{5}$$

where k_{el}^t is the tangential spring stiffness coefficient, k_{diss}^t is the tangential damping one, $\overline{t}_{ij}$ is the tangential vector which is perpendicular to $\overline{n}_{ij}$, and $\overline{\delta}_{\text{t}}$ is the tangential contact displacement vector. In the nonlinear models implemented in the DEM module, in particular, k_{el}^t is calculated based on the Mindlin and Deresiewicz (MD) theory. The estimated tangential force models included in the DEM module are indicated in Table 2.

In Table 2, it is worth noticing that η_t is the damping coefficient associated with a specific model, G_{eff} is the effective shear modulus, and m_{eff} is the effective mass. Furthermore, μ is the sliding friction coefficient, $\delta_{t,\,\max}$ is the displacement at which sliding starts [30, 31], and C_t is the correction factor for the ZZYt model [28].

In addition, using the classical Coulomb's law of friction, the tangential force vector $\overline{f}_{ij}^t$ is defined by [33],

$$f_{\text{C}} = \mu \left| \overline{f}_{ij}^n \right| = \mu f^n, \tag{6}$$

$$\overline{f}_{ij}^t = -\min\left(f_{\text{C}}, \left| \overline{f}_o^t \right| \right) \overline{t}_{ij}, \tag{7}$$

where f_C is the Coulomb force, and f^n is the normal force modulus. A different approach utilized to compute the tangential force vector is the one based on the method of Maw et al. [34]. This method, which has also been used in the past by Tsuji et al. [27], is based on limiting both the tangential deformation and the tangential force by changing the tangential deformation. More specifically, when sliding friction occurs, the tangential deformation is limited in this case according to [27],

$$\overline{\delta}_t = \frac{f_{\text{C}} \overline{t}_{ij}}{k_t} \tag{8}$$

Since it improves the particle response when there are collisions involving a sliding condition, this correction has been employed in this work.

2.4 Tangential contact displacement correction

The tangential contact displacement $\left(\overline{\delta}_t\right)$ and the tangential component of the relative velocity $\left(\overline{v}_{ij}^t\right)$ are not necessarily parallel vectors. Therefore, in the soft body approach, the tangential contact displacement must be corrected as follows

Table 2 Estimated tangential force models included in the CFLOWSS DEM module

Estimated tangential force model	k_{el}^t	k_{diss}^t
Linear spring dashpot model (LSD) [14]	k_t	η_t
Di Renzo and Di Maio (DDt) [29]	$\frac{16}{3} G_{\text{eff}} \sqrt{R_{\text{eff}}} \delta_n^{1/2}$	η_t
Langston, Tüzün and Heyes (LTHt) [30, 31]	$\lvert\overline{\delta}_t\rvert = \min\left(\lvert\overline{\delta}_t\rvert,\ \delta_{t,\max}\right)$ $\mu\lvert\overline{f}_{ij}^n\rvert\left[1-\left(1-\frac{\lvert\overline{\delta}_t\rvert}{\delta_{t,\max}}\right)^{3/2}\right]\frac{1}{\lvert\overline{\delta}_t\rvert}$	$\eta_t\left(6m_{\text{eff}}\mu\lvert\overline{f}_{ij}^n\rvert\frac{\sqrt{1-\lvert\overline{\delta}_t\rvert/\delta_{t,\max}}}{\delta_{t,\max}}\right)^{1/2}$
Zheng, Zhu, and Yu (ZZYt) [28]	$\lvert\overline{\delta}_t\rvert = \min\left(\lvert\overline{\delta}_t\rvert,\ \delta_{t,\max}\right)$ $\mu\lvert\overline{f}_{ij}^n\rvert\left[1-\left(1-\frac{\lvert\overline{\delta}_t\rvert}{\delta_{t,\max}}\right)^{3/2}\right]\frac{1}{\lvert\overline{\delta}_t\rvert}$	$C_t\frac{\eta_1}{2G_i\delta_{t,\max}}\left(1.5\mu\lvert\overline{f}_{ij}^n\rvert\sqrt{1-\frac{\lvert\overline{\delta}_t\rvert}{\delta_{t,\max}}}\right)^{\frac{1}{2}}$

[12]:

$$\overline{\delta}_t^{nc} = \int_{t_0}^{t} \overline{v}_{ij}^t \mathrm{d}t \leftarrow \text{Not corrected} \tag{9}$$

$$\overline{\delta}_t = \overline{\delta}_t^{nc} - \left(\overline{n}\cdot\overline{\delta}_t^{nc}\right)\overline{n} \leftarrow \text{Corrected} \tag{10}$$

In this work, to carry out the referred correction, the tangential displacement history is stored in the vector $\overline{\delta}_t$. For a given pair contacting bodies, thus, this vector is updated at each time step from the beginning of the contact until the contact is ended. Mathematically, $\overline{\delta}_t$ is given by [12],

$$\overline{\delta}_{t,i}^{*} = \overline{\delta}_{t,i-1} + \overline{v}_{t,i}\Delta t_i, \tag{11}$$

$$\overline{\delta}_{t,i} = \overline{\delta}_{t,i}^{*} - \left(\overline{n}_i\cdot\overline{\delta}_{t,i}^{*}\right)\overline{n}_i, \tag{12}$$

where Δt_i is the time step, $\overline{\delta}_{t,i}^{*}$ is the not corrected tangential displacement history vector, and the subscript i indicates the current time step.

A different way of correcting the tangential displacement history vector is using a scalar-based approach. In this second approach, the tangential vector $\overline{t}_i$ and a scalar representing the tangential displacement δ_t are saved. Mathematically, $\overline{\delta}_t$ is calculated in this case as,

$$\overline{\delta}_{t,i} = \text{sign}\left(\overline{t}_{i-1},\ \overline{t}_i\right)\delta_{t,i}\overline{t}_i + \overline{v}_{t,i}\Delta t_i, \tag{13}$$

where $\text{sign}\left(\overline{t}_{i-1},\ \overline{t}_i\right)$ takes the value of 1 when $\overline{t}_{i-1}$ and $\overline{t}_i$ are almost (considering a threshold) pointing in the same direction. If the opposite is true, $\text{sign}\left(\overline{t}_{i-1},\ \overline{t}_i\right)$ takes the value of -1. This algorithm just aligns $\overline{\delta}_{t,i-1}$ with the actual tangential vector $\overline{t}_i$. For a relatively small number of particles, no significant differences in the results obtained with this second approach and the one described in [12] were observed. Notice that in this work, for the tangential contact displacement correction, the first approach (Eqs. (11)–(12)) has been employed. Finally, it is worth highlighting that there is no a correction on the normal direction because by definition, the normal contact displacement is always parallel to the normal vector, and there is no a history component.

2.5 Explicit timestep solver

Finally, to solve in time the models described in Sect. 2, the solver used in the CFLOWSS DEM module employs a forward Euler's method. That is, starting from an initial condition, for instance, next timestep particle positions and velocities are computed from,

$$\overline{x}_{i+1} = \overline{x}_i + \overline{v}_i\Delta t_i, \tag{14}$$

$$\overline{v}_{i+1} = \overline{v}_i + \overline{a}_i\Delta t_i, \tag{15}$$

where $\overline{a}_i$ represents the sum of forces coming from particles contact and the gravitational field. All models discussed here have been implemented in the CFLOWSS DEM module. The details of referred implementation are summarized in next section.

3 DEM module Implementation

The DEM model described in Sect. 2 has been implemented as a module in the in-house computational package CFLOWSS [20–23]. Some details of the referred module implementation are provided in Sect. 3. Notice that CFLOWSS aims to numerically solve complex flows including particulate/granular flows and mineral-slurries. Currently, different Eulerian- and Lagrangian-based approaches are being implemented in this large package. Specific Lagrangian techniques accounted for include discrete element methods (DEM) and smoothed particle hydrodynamics (SPH) [35]. In addition, DEM approaches have also been

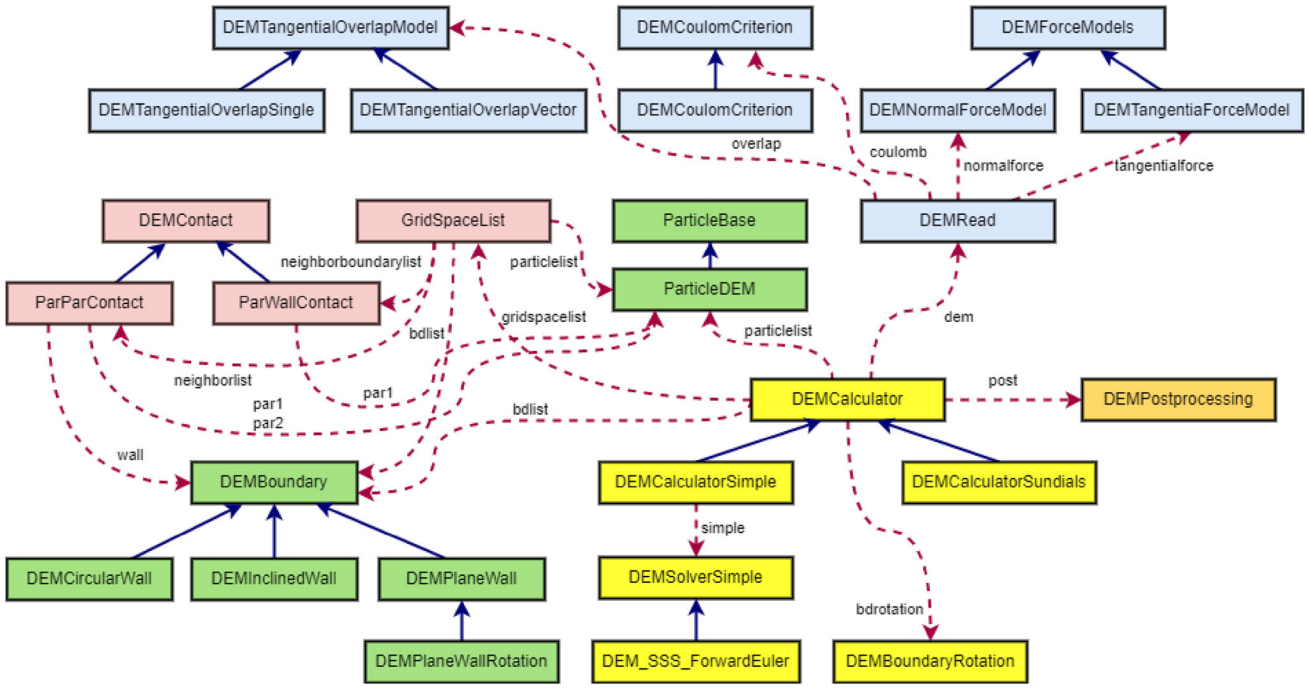

Fig. 1 Simplified view of DEM module class hierarchy in CFLOWSS package. Boxes represent classes and dark blue arrows inheritance relations. Purple dashed arrows are used in turn to highlight links between classes and variables involved. Colors used in boxes indicate domain (green), model (blue), simulation (yellow), contact (red), and output (orange) classes. (Color figure online)

included in CFLOWSS due to their applicability to solving particulate flows in large-scale industry including mining [36].

3.1 DEM module class hierarchy

The CFLOWSS package is being developed using an object-oriented programming (OOP) paradigm and C++ as the main programming language. Accordingly, the main class of the CFLOWSS DEM module is the DEMCalculator one. As highlighted in Fig. 1, this class includes several key attributes like a DEMRead object, a GridSpaceList object, a DEMPostprocessing object, and arrays of ParticleDEM and DEMBoundary objects. The normal (DEMNormalForceModel) and tangential (DEMTangentialForceModel) force models, as well as the friction (DEMCoulomCriterion) and tangential overlap correction (DEMTangentialOverlapModel) ones are contained inside the DEMRead class. Additionally, this class contains the DEM problem settings that are read from an input file. DEM particles are represented by the ParticleDEM class and DEM boundaries by the DEMBoundary one. A linked cell method has been implemented in the GridSpaceList class, and particle contacts are defined with the DEMContact ones. The objects referred to as static or moving rigid boundaries are defined in the DEMBoundary class. To entirely describe the rotation of one or several boundaries, the DEMBoundaryRotation class is utilized. The simple forward Euler's method used to obtain DEM solutions at each time step is implemented in the DEM_SSS_ForwardEuler class. Finally, DEM output files are generated using the object DEMPostprocessing class. These output files are finally utilized for postprocessing purposes in tools such as ParaView [37].

Notice that Fig. 1 shows a simplified view of the class hierarchy characterizing the new CFLOWSS DEM module. In this figure, in particular, boxes represent classes, and the different colors indicate (computational) domain (green), model (blue), simulation (yellow light), contact (red), and output (yellow dark)-related classes. Computational domain classes define the physical domain accounted for in the simulations and include moving particles (ParticleBase and ParticleDEM) and physical boundaries (DEMBoundary). Finally, as highlighted Table 3, all the physical models described in Sect. 2 have specific classes associated with them.

3.2 DEM module solution approach

When using the CFLOWSS DEM module discussed in this work, at each time step, the solution to a Lagrangian problem involving soft particles is obtained in several stages. As shown in Fig. 2, using a neighbor searching approach based on the linked cell method [20], particle collisions are first

Table 3 Relationship between C++ classes and models/equations included in the new DEM module implemented in CFLOWSS

Class	Models/equations
DEMTangentialOverlapSingle	Correction of the tangential displacement history vector using a scalar-based approach—Eq. (13)
DEMTangentialOverlapVector	Correction of the tangential displacement history vector using a scalar-based approach—Eqs. (12, 13)
DEMCoulomCriterion	Limited tangential deformation and tangential force—Eq. (8)
DEMNormalForceModel	Normal force models—Table 1
DEMTangentialForceModel	Tangential force models—Table 2

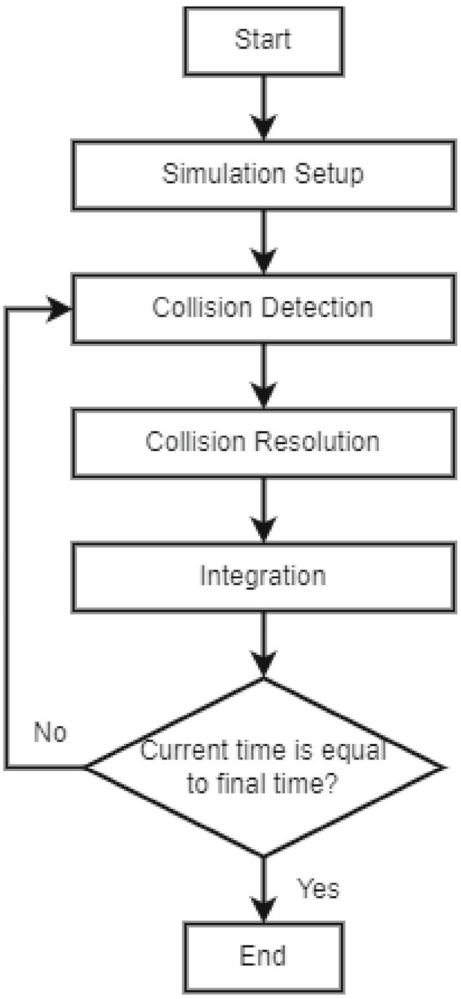

Fig. 2 DEM module solution approach

Table 4 Parameters used in the experiments performed by Xu et al. [38]

Parameter	Symbol	Value
Length (mm)	L	64.0
Diameter of cylinder (mm)	D	241.0
Size of glass beads (mm)	d	10.14
Number of particles	n_p	600 black plus 600 green glass beads
Rotation velocities (RPM)	n	20, 40, 60, 80

detected. Once a particle contact is found, normal and tangential forces are calculated next using the different models described in Sect. 2. After doing so, new particle positions and velocities (linear and angular) are computed using the forward Euler's method. Finally, when the current time is equal to the final one, the numerical simulation comes to an end; otherwise, the solution stages indicated above are repeated in the next time step.

4 Results and discussions

The mains results obtained in this work are discussed in this section. The referred discussion is carried out considering first qualitative aspects, and then quantitative ones.

4.1 Qualitative results

The verification and validation of the CFLOWSS DEM module discussed in this work has been carried out accounting for both the experimental results discussed by Xu et al. [38] and the numerical ones obtained using a commercial DEM software [24]. The main parameters accounted for in the experimental work [38] used as reference here are summarized in Table 4. In particular, as illustrated in Fig. 3, the rotating drum is filled with 600 black glass beads plus 600 green ones. In addition, four rotation velocities are considered, 20, 40, 60, and 80 RPM. In turn, for obtaining the numerical results used for comparison purposes here, a well-known commercial DEM software (EDEM) [18, 24, 39] was utilized.

To carry out the numerical simulations, the material properties for the glass beads and the Perspex cylinder were taken from the works by Xu et al. [38] and Li et al. [40]. These property values are shown in Table 5. It is worth noticing here that the sliding friction plays an important role in describing the physics happening inside tumbling mills. According to Li et al. [40], the sliding friction coefficient between the Perspex cylinder and the glass beads is equal to 0.1333. When

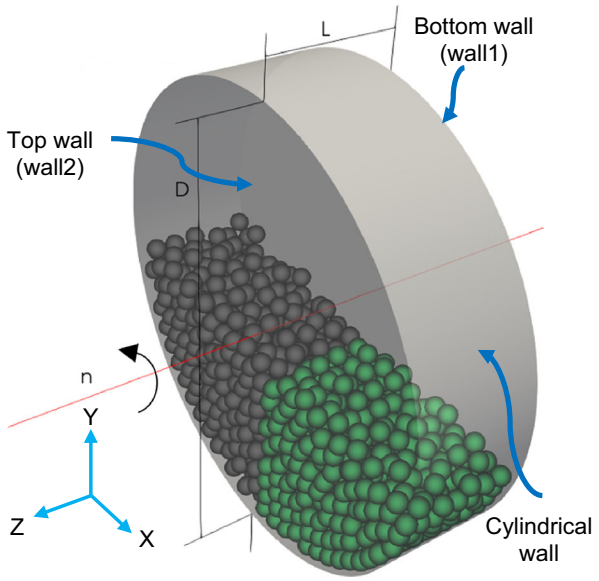

Fig. 3 Rotating drum representation with glass beads

Table 5 Material properties for glass beads and Perspex cylinder

Properties	Symbol	Glass beads	Perspex cylinder
Density (kg/m^3)	ρ	2.456E+03	
Young's modulus (Pa)	E	55.0E+09	200.0E+09
Poison ratio (−)	υ	0.25	0.3
Sliding friction coefficient with glass beads (−)	μ	0.1545	1.0
Normal restitution coefficient with glass beads (−)	e_n	0.972 (*)	0.8 (*)

*Values estimated from Lorenz et al. [41]

this sliding friction coefficient value was used in the numerical simulations performed in this work, the flow behavior was different to that described in the original experimental work [38]. More specifically, it was noticed that the friction force is not strong enough to produce the tumbling movement observed experimentally. Increasing this value improved the physical behavior inside the rotating drum and the particulate flow behaved qualitatively more similar to the experimental photographs provided in [38]. Notice that real glass beads often differ from those numerically formed considering perfect spherical particles, so the latter might lead to an underestimation of the shear strength of the bead packing. This aspect was not assessed in this work. Instead, different sliding friction coefficient values were tried, and it was found that a value equal to 1.0 gives the best agreement of the numerical results with the experimental ones. Therefore, in all numerical simulations (including EDEM simulations) carried out in this work, a sliding friction coefficient between the cylinder and the glass beads equal to 1.0 was employed. Notice as well that in the work of Xu et al. [38], a value of 0.57 was used for this coefficient in order to have a better agreement between the 2D simulation and the experimental results.

For the CFLOWSS DEM module, the simulation parameters accounted for included a time step equal to 10^{-6} s, a total simulation time of 12 s, the linked cell neighborhood method for the data structure, the tangential contact displacement correction using the vectors (Eqs. 11 and 12), the TTIn normal force model and the DDt tangential one. Notice that the TTIn normal force model employed a damping coefficient η_n calculated using other material properties, according to $\eta_n = \frac{-2.2664 \ln(e_n)\sqrt{m_{\text{eff}} k_{\text{Hertz}}}}{\sqrt{\ln(e_n)^2 + 10.1354}}$ [32], whereas the DDt tangential model used a $\eta_t = 0$. Similar parameters are used for the EDEM simulations but the contact model selected was Hertz–Mindlin with JKR cohesion due to its efficient and accurate force calculation. No rolling friction model was considered for the EDEM simulations. CFLOWSS DEM module and EDEM considered an initialization where the particles were released and allowed to stabilize for approximately 2 s.

Accordingly, Fig. 4 shows the original experimental results (photographs) discussed in Xu et al. [38], and the numerical ones obtained using EDEM [24] and the CFLOWSS DEM module. All these results correspond to a drum rotation velocity equal to 20 RPM. As it can be observed from Fig. 4, the CFLOWSS results show a relatively good qualitative agreement with both the experimental photographs and the numerical results obtained using EDEM. More specifically, the position and dispersion of the black and green balls inside the tumbling mill characterizing the experiments are similar to those ones associated with the CFLOWSS results at different time steps. Similarly, both CFLOWSS and EDEM simulation results are qualitatively similar in shape and dispersion of particles inside the tumbling mill.

In turn, Fig. 5 shows another qualitative comparison of the results obtained using the CFLOWSS DEM module and the experimental results from Xu et al. [38] and those ones obtained with the EDEM software [24]. The comparison is carried out in this case in terms of the bed surface shape (and inclination angle) accounting for a fixed time equal to 10.88 s. As observed from Fig. 5, the bed surface shapes described by the CFLOWSS DEM module are similar to those obtained using EDEM and the bed shapes determined experimentally. At 80 RPM, however, due to the high velocity of the particles and the measurement techniques employed, the experimental image is very diffuse. Therefore, at this rotation speed, only numerical results obtained with CFLOWSS and EDEM

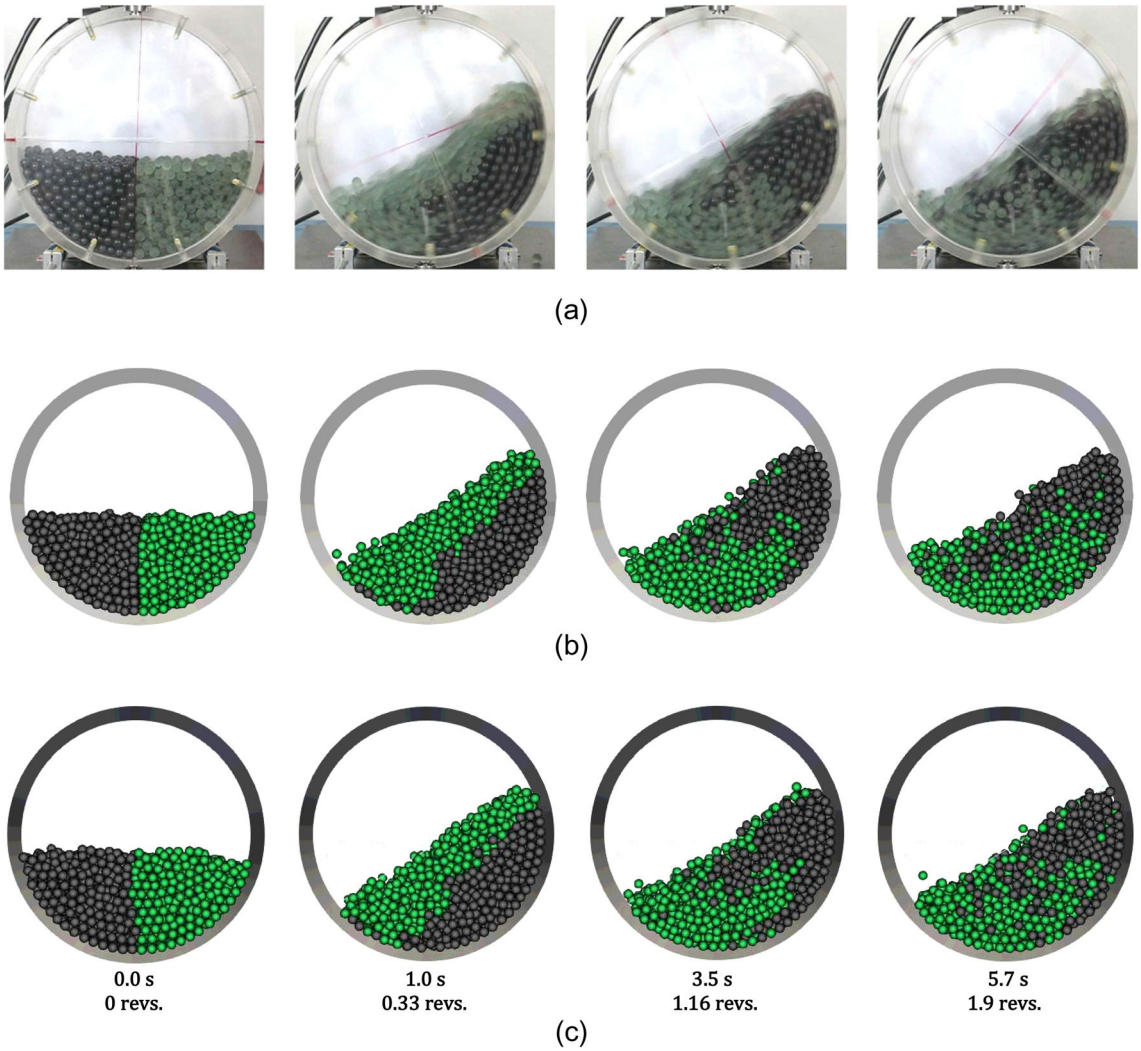

Fig. 4 Qualitative results at 20 RPM. **a** Experimental photographs from Xu et al. [38], **b** EDEM numerical results, and **c** CFLOWSS numerical results

will be compared each other. Overall, according to Fig. 5, for the four drum rotation speeds accounted for, the CFLOWSS and EDEM results are qualitatively similar. In addition, at 60 RPM, the experimental results have balls moving at higher positions than the numerical results. Notice that at a different time ($t = 5.4$) (not shown here for the sake of brevity), these balls are not present in the experimental results, and a relatively similar bed surface is observed compared with the numerical results. Finally, Fig. 5 highlights that at 20 and 40 RPM, the bed surfaces formed experimentally and the corresponding ones obtained using both the CFLOWSS DEM module and EDEM are very close.

In the past, several research works have carried out qualitative comparisons as those discussed in Sect. 4.1. However, due to lack of quantitative values characterizing each set of results, this sort of qualitative comparisons can be misleading. Therefore, an effort has been made in this work to quantify the numerical results obtained with the CFLOWSS DEM module under discussion here. These quantitative results are discussed in the following section.

4.2 Quantitative results

Initially, a comparison of the upper angles of repose at different drum rotation speeds was also carried out as a means of quantitative verification of the results obtained in this work. These upper angles of repose represent the angle at which particles on the bed surface begin to slow down forming an avalanche. The way that the referred angles of repose were measured is shown in Fig. 5. Notice however that, at 80 RPM, the angles of repose were not considered due to the flow complexity and because the experimental image is very diffuse. Accordingly, the angles of repose determined for drum rotation speeds of 20, 40 and 60 RPM are summarized in Table 6.

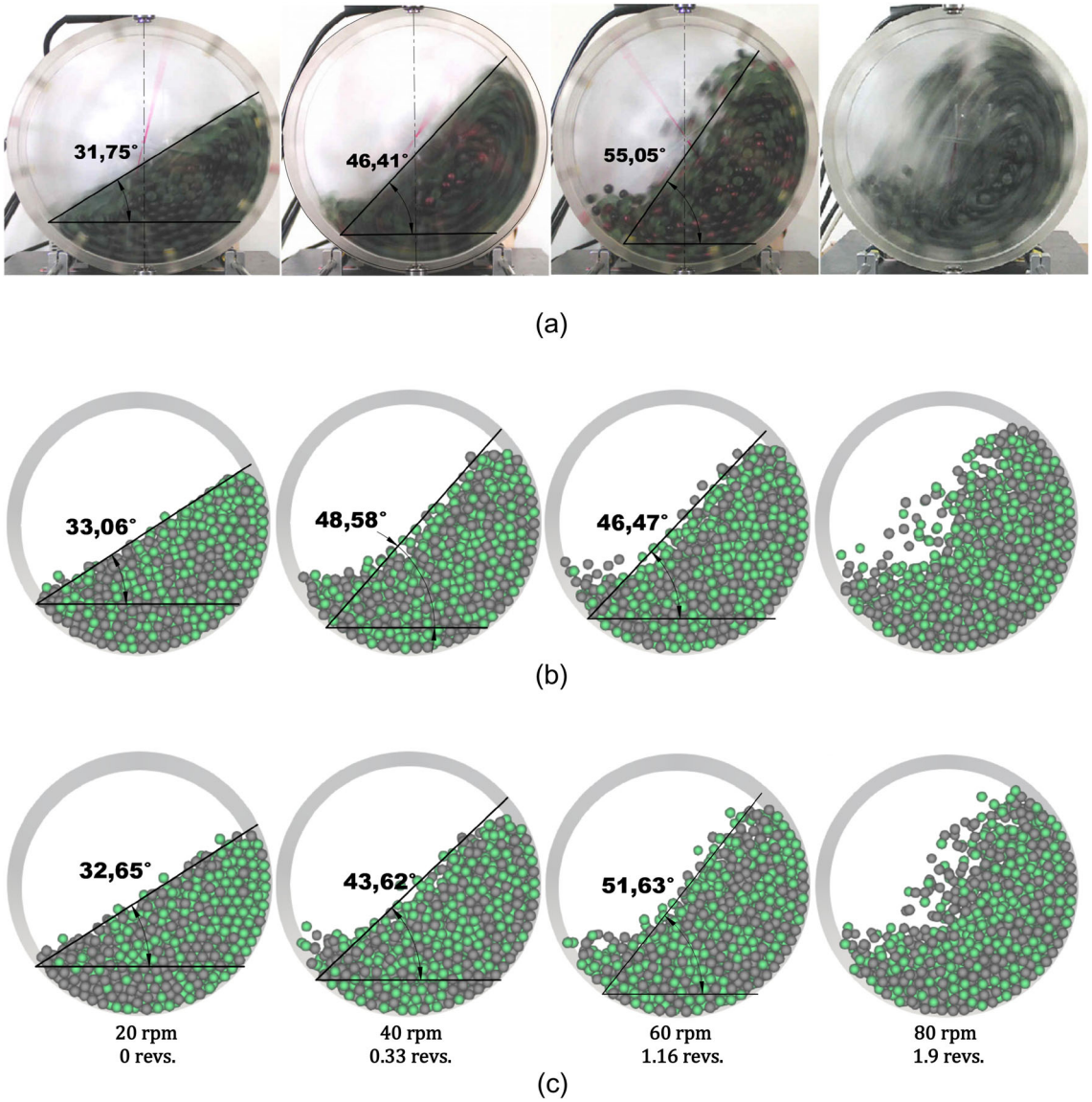

Fig. 5 Qualitative results at 20, 40, 60 and 80 RPM for a fixed time equal to $t = 10.88$ s. **a** Experimental photographs from Xu et al. [38], **b** EDEM numerical results, and **c** CFLOWSS numerical results

Table 6 Upper angles of repose for the experimental results by Xu et al. [38] and the numerical ones obtained using the CFLOWSS DEM module and the EDEM software [24]

Rotation speed (RPM)	Experimental (Xu et al. [38])	EDEM	CFLOWSS
20	31.75	33.06	32.65
40	46.41	48.58	43.62
60	45.5	46.47	46.3

More specifically, at 20 RPM, compared to the experiments, the numerical results slightly overestimate the upper angle of response, but when compared each other, they are quite alike. A similar scenario is observed at 60 RPM, but this time, the discrepancies between the experimental and numerical results are even smaller. Finally, at 40 RPM, the referred discrepancies increase slightly. Overall, the average discrepancies between the experimental and numerical results are about 3%.

For parameters such as number of contacts, forces, and torques, there are no quantitative results available in the experimental work by Xu et al. [38]. Therefore, the quantitative analyses discussed in the remaining of this section are restricted to numerical results only. More specifically, a quantitative comparison of the results obtained with the CFLOWSS DEM module, and those produced by EDEM has been carried out. In order to do so, statistical analyses of

the number of contacts, forces, and torques developed on the cylinder over time have been performed. In such analyses, all four rotation velocities (20, 40, 60, and 80 RPM) studied in the experimental work by Xu et al. [38] have been accounted for. For the sake of brevity, however, only the results for the lowest and the highest rotation velocities accounted for, 20 RPM and 80 RPM, respectively, are discussed in detail here. The results associated with the other two velocities are discussed in comparative terms only.

Accordingly, Fig. 6 shows the quantitative results obtained accounting for the lowest rotation velocity studied in this work, 20 RPM. More specifically, in Fig. 6a, b, the number of (i) contacts of all kinds (all–all), (ii) contacts between black or green particles (par–par), (iii) and contacts between the particles and the cylinder (par–wall) predicted by EDEM and CFLOWSS, respectively, is shown. It can be observed from these plots that the temporal evolution of the number of contacts predicted by both EDEM (Fig. 6a) and CFLOWSS (Fig. 6b) is quite similar. These temporal profiles start, indeed, with a relatively high number of contacts (at the beginning of the drum rotation) and then their associated values change rapidly and remain relatively stable until the end of the simulation. Similarly, Fig. 6c, d shows, respectively, the temporal evolution of (i) the power generated by the axial torque exerted by the particles on the cylinder along the direction of drum rotation (power), (ii) the force along the y direction applied by the particles to the cylindrical wall of the rotating drum (cylinder force y), and (iii) the force along the z direction exerted on the top wall of the rotating drum (top wall force z) predicted by EDEM and CFLOWSS. As observed from these plots, the temporal profiles described by both solvers are similar as well.

To remove some of the fluctuations present in the instantaneous profiles described before, a statistical treatment based on a moving average technique accounting for about 50 points has been utilized in this work. The outcomes from the application of this average technique are illustrated in Fig. 6e, f. In particular, it is noticed that the moving average applied to the number of contacts predicted by EDEM and CFLOWSS (Fig. 6e) produces curves featuring the same trends, although with some acceptable discrepancies (less than 7.52% considering the mean value) among their characteristic values. As expected, when using a moving average, the large number of peaks and valleys characterizing the instantaneous power and forces profiles (Fig. 6c, d) are greatly smoothed (Fig. 6f). Specifically, the torque and forces average profiles associated with EDEM and CFLOWSS are very close each other and converge to similar values. To complement the results discussed so far, boxplots have also been generated using the EDEM and CFLOWSS predictions. Therefore, Fig. 6g, h shows, respectively, boxplots for the number of contacts and the power/forces numerically predicted. From these last results, compared to EDEM, CFLOWSS seems to predict a relatively smaller number of contacts, regardless of the kind of contact (all–all, par–par, and par–wall) (Fig. 6g). Compared to the results produced by EDEM, in terms of the median characterizing the number of contacts of the type all–all, the relative discrepancy of the CFLOWSS ones (called just relative discrepancy henceforth) is about 8.2%. For the median of power, in turn, the CFLOWSS relative discrepancy is about 2.4%. These levels of discrepancy between the EDEM and CFLOWSS results are considered acceptable for the purposes of this work.

The same quantitative analysis performed for the lowest rotation velocity (20 RPM) has also been performed for the highest one, 80 RPM, Fig. 7. As at the 20 RPM case, it can be observed that for a 80 RPM drum rotation velocity, the instantaneous profiles related to the number of contacts for both EDEM (Fig. 7a) and CFLOWSS (Fig. 7b) have similar shapes and seem to converge to similar values. It is also noticeable that compared to the results obtained at 20 RPM, the profiles are more uniform, and the peaks and valleys are relatively smaller. Contrarily, like at 20 RPM case, the temporal profiles characterizing the power and forces exerted by the particles on the rotating drum (Fig. 7c, d) present large fluctuations and many peaks and valleys. In addition, as it is noticed from Fig. 7e, f, respectively, the profiles associated with the moving average of number of contacts and forces are converging to a relatively linear line. Nevertheless, the power curves shown in Fig. 7f oscillate more than the 20 RPM corresponding ones (Fig. 6f). This seems to be associated with the relatively higher impact velocities (Fig. 7c, d) characterizing the cataracting regimen of the particulate flow developed inside the rotating drum. These increased particle velocities produce relatively high impact forces that lead to high momentums over the drum, which are finally responsible for the torque and power demanded. Figure 7g, h shows, in turn, boxplots associated with the CFLOWSS and EDEM predictions at 80 RPM. It is observed from Fig. 7g that the CFLOWSS and EDEM results have similar boxplots, which implies that both numerical simulations predict similar number of contacts in almost 50% of the data. Compared to EDEM, CFLOWSS also seems to predict a relatively higher number of contacts of all kinds (all–all, par–par, and par–wall). Indeed, the CFLOWSS relative discrepancy associated with the median of the all–all number of contacts is about 2.9%, which is lower than the one observed at the 20 RPM case (8.2%).

To avoid being repetitive, the results obtained accounting for the other two drum rotation velocities studied here (40 and 60 RPM) will not be discussed separately here. Instead, all four rotation velocities related results will be addressed together. Thus, Fig. 8 shows a summary of the quantitative results obtained at 20, 40, 60, and 80 RPM using both EDEM and CFLOWSS. In particular, it can be observed from Fig. 8a,

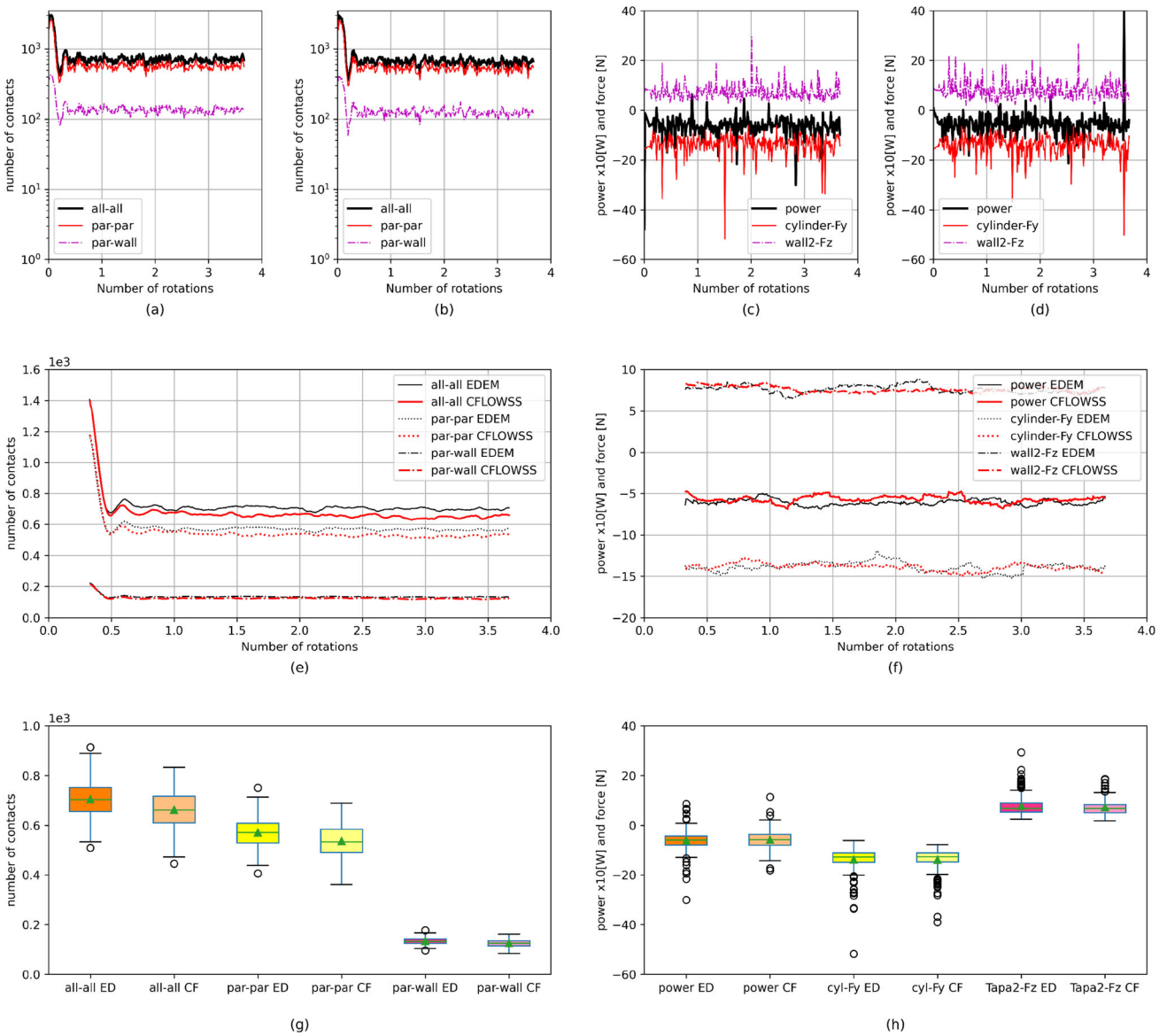

Fig. 6 Quantitative results at 20 RPM. **a** EDEM and **b** CFLOWSS evolution as a function of the number of drum rotations of all–all, particle–particle, and particle–wall contacts. **c** EDEM and **d** CFLOWSS evolution as a function of the number of drum rotations for power consumption [W] scaled by $\times 10$, force [N] over the cylinder along the y direction, and force [N] over the cylinder top along the z direction. **e** EDEM and CFLOWSS number of contacts moving average. **f** EDEM and CFLOWSS power and forces moving average. **g** EDEM (ED) and CFLOWSS (CF) boxplots for number of contacts. **h** EDEM (ED) and CFLOWSS (CF) boxplots for power and forces

b that both the all–all number of contacts and the profile oscillations decrease when the drum rotation velocity increases. These decreases can be associated with the intense movement of particles that occur inside rotating drums at high velocities, which causes the dispersion of particles. On the contrary, Fig. 8c, d, h shows that the power consumption oscillations increase with the increase in the drum rotation velocity. The relatively larger peaks and valleys observed when the rotation velocity increases are due to the instantaneous large forces resulting from the impact on the drum of particles or groups of particles with an increased velocity.

The moving average of the number of all–all contacts predicted by both EDEM and CFLOWSS at different rotation velocities is shown in Fig. 8e. It can be observed from this figure that the CFLOWSS DEM module seems to predict a number of contacts slightly lower that EDEM especially at low rotation speeds. Overall, however, the agreement between both number of contact-related predictions is relatively good. The same does not occur in the case of the

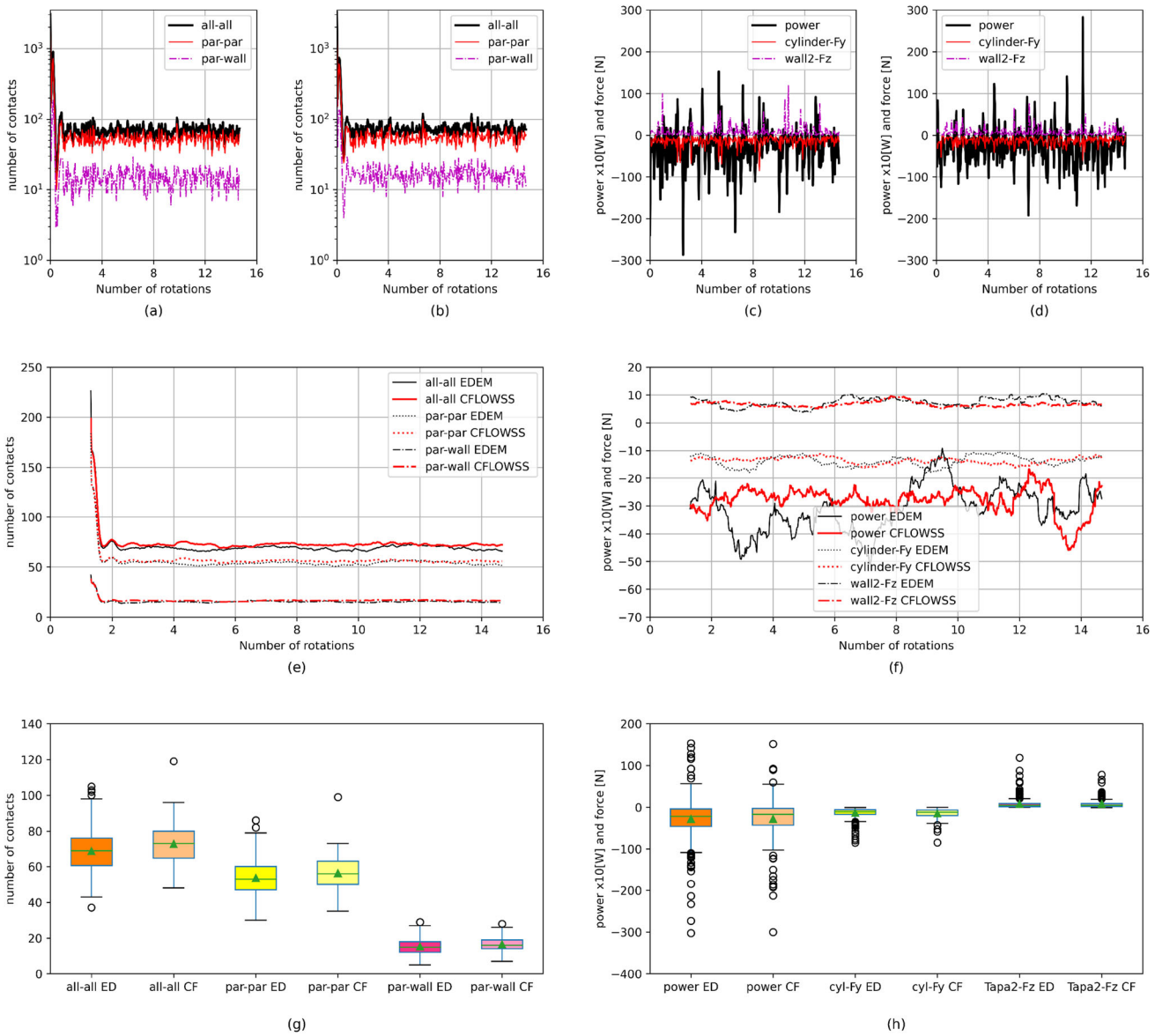

Fig. 7 Quantitative results at 80 RPM. **a** EDEM and **b** CFLOWSS evolution as a function of the number of drum rotations of all–all, particle–particle, and particle–wall contacts. **c** EDEM and **d** CFLOWSS evolution as a function of the number of drum rotations for power consumption [W] scaled by $\times 10$, force [N] over the cylinder along the y direction, and force [N] over the cylinder top along the z direction. **e** EDEM and CFLOWSS number of contacts moving average. **f** EDEM and CFLOWSS power and forces moving average. **g** EDEM (ED) and CFLOWSS (CF) boxplots for number of contacts. **h** EDEM (ED) and CFLOWSS (CF) boxplots for power and forces

powers' moving average (Fig. 8f). In terms of drum power consumption, indeed, the discrepancies in the EDEM and CFLOWSS moving average values increase with the increase in the drum rotation velocity due to the high and oscillating instantaneous values (Fig. 8c, d). This is somehow an expected result because power consumption is a second-order parameter that depends on other first-order ones such as particle velocity and force. Of course, the power consumption absolute value increases as the rotation velocity does so. From the boxplots related with the number of all–all contacts (Fig. 8g), in turn, it is noticed that the interquartile ranges, as well as the minimum and maximum values characterizing the EDEM and CFLOWSS predictions, are similar, which indicate that the predicted results are almost symmetrical. The number of outliers seems to be small, and the CFLOSSS boxplots are located at a position slightly lower than the EDEM ones, especially for small rotation velocities. Besides, the EDEM and CFLOWSS relative discrepancies decrease as the drum rotation velocity increases. At 60 RPM, indeed, these discrepancies reach a minimum value of 0.8%. Finally,

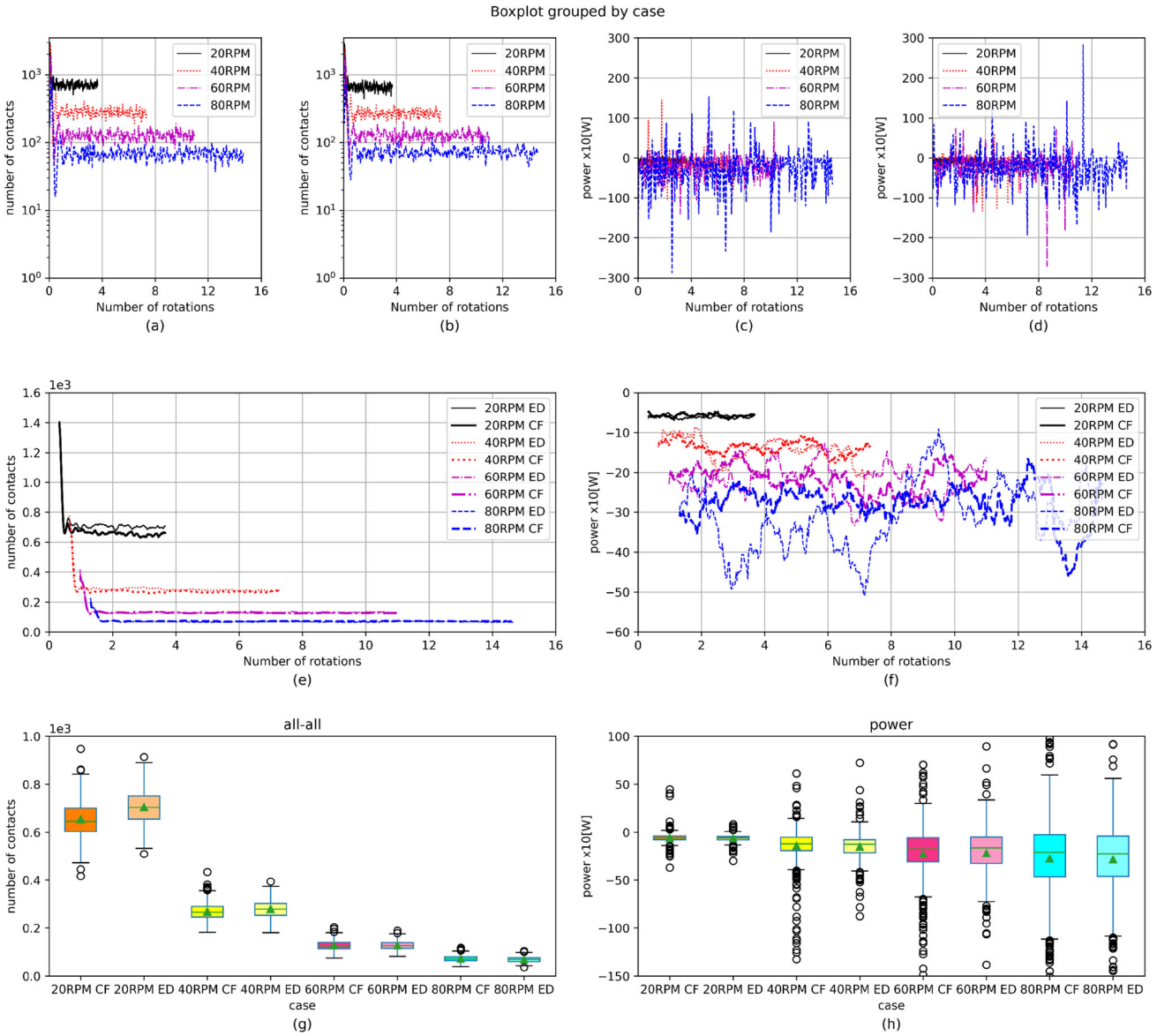

Fig. 8 Summary of quantitative results obtained at 20, 40, 60, and 80 RPM. **a** EDEM and **b** CFLOWSS number of all–all contacts. **c** EDEM and **d** CFLOWSS power consumption [W] scaled by $\times 10$. **e** EDEM and CFLOWSS number of all–all contacts moving average. **f** EDEM and CFLOWSS power moving average. **g** EDEM (ED) and CFLOWSS (CF) boxplots for number of all–all contacts. **h** EDEM (ED) and CFLOWSS (CF) boxplots for power

Fig. 8h shows boxplots associated with the drum power consumption. It is observed from this last figure that both EDEM and CFLOWSS boxplots are similar. Specifically, due to the relatively high instantaneous contact forces, there are a lot of outliers especially at high rotation velocities. In addition, in terms of the median of the drum power consumption, the CFLOWSS relative discrepancies increase with the increase in the rotation velocity. At 80 RPM, these discrepancies reach a maximum value of 7.4%.

5 Conclusions

Using a new DEM tool that is one of the modules of a larger in-house computational package called CFLOWSS, particulate flows in rotating drums were qualitatively and quantitatively analyzed in this work. The results from such analyses were compared with experimental ones and other numerical results obtained using a commercial DEM software, EDEM. In qualitative terms, the CFLOWSS results showed a relatively good agreement with experimental photographs previously taken in a laboratory. More specifically,

the position and dispersion of the black and green balls characterizing the experiments were similar to those ones associated with the CFLOWSS results at different time steps. In quantitative terms, in turn, the CFLOWSS DEM module predictions showed a strong correspondence with the EDEM ones. For instance, the relative discrepancies of the boxplots' medians associated with the number of contacts, power, and forces predicted by EDEM and CFLOWSSS presented values smaller than 8%. At 60 RPM, indeed, the number of contact-related discrepancies reached values as low as 0.8%. This outcome highlights that the DEM tool discussed in this work is capable of producing results with accuracies similar to well-known commercial software like EDEM. To analyze quantitatively DEM results, statistical treatments such the one used here are barely employed. The work carried out here emphasizes, however, that this sort of assessment provides an improved way to analyze the behavior of particulate flows.

Acknowledgements This work has been funded by CONCYTEC-FONDECYT (PROCIENCIA) (Peru) and the World Bank with contract No. 155-2018-FONDECYT-BM-IADT-AV, contract No. 015-2021-FONDECYT (ECOS NORD-PERU) and contract No. 10-2018-FONDECYT/BM-PROGRAMAS DE DOCTORADOS EN AREAS EXTRATÉGICAS Y GENERALES. This work has been also supported by the Engineering Doctoral program at "Pontificia Universidad Católica del Perú" (PUCP).

Declarations

Conflict of interest On behalf of all authors, the corresponding author states that there is no conflict of interest.

References

1. Fuerstenau MC, Han KN (2003) Principles of mineral processing, littleton. SME, Colorado
2. Napier-Munn T (2015) Is progress in energy-efficient comminution doomed? Min Eng 73:1–6
3. Engeco (2021) Mining energy consumption 2021
4. Musa F, Morrison R (2009) A more sustainable approach to assessing comminution efficiency. Min Eng 22:593–601
5. Kloss C, Goniva C, Hager A, Amberger S, Pirker S (2012) Models, algorithms and validation for opensource DEM and CFD-DEM. Prog Comput Fluid Dyn 12(2/3):140–152
6. Brennen CE (2014) Fundamentals of multiphase flow. Cambridge University Press
7. Chou H-T, Lee C-F (2009) Cross-sectional and axial flow characteristics of dry granular material in rotating drums. Granul Matter 11(1):13–32
8. Rao KK, Nott PR (2008) An introduction to granular flow. Cambridge University Press, Cambridge
9. Ding Y, Forster R, Seville J, Parker D (2002) Granular motion in rotating drums: bed turnover time and slumping–rolling transition. Powder Technol 124:18–27
10. Mellmann J (2001) The transverse motion of solids in rotating cylinders—forms of motion and transition behavior. Powder Technol 118:251–270
11. Beke B (1981) Tumbling mill mechanics. The Process of Fine Grinding, pp 74–83
12. Fleischmann J, Serban R, Negrut D, Jayakumar P (2016) On the importance of displacement history in soft-body contact models. J Comput Nonlinear Dyn 11(4):044502
13. Pazouki A, Kwarta M, Williams K, Likos W, Serban R, Jayakumar P, Negrut D (2017) Compliant contact versus rigid contact: a comparison in the context of granular dynamics. Phys Rev E 96(4):042905
14. Cundall P, Strack O (1979) A discrete numerical model for granular assemblies. Géotechnique 29:47–65
15. Dubois F, Acary V, Jean M (2018) The contact dynamics method: a nonsmooth story. Comptes Rendus Mécanique 346(2):247–262
16. Moreau JJ, Panagiotopoulos PD (2014) Nonsmooth mechanics and applications. Springer, Berlin
17. Moreau JJ, Jean M (1996) Numerical treatment of contact and friction: the contact dynamics method. Eng Syst Design Anal Conf 4:201–208
18. EDEM (2014) EDEM Theory Reference Guide, Edinburgh: DEM Solutions
19. ESSS (2023) https://rocky.esss.co/software/?tab=overview, ESSS, 2023. [En línea]. Available: https://rocky.esss.co
20. Angeles L, Celis C (2019) Assessment of neighbor particles searching methods for discrete element method (DEM) based simulations. In: de VI international conference on particle-based methods: fundamentals and applications, Barcelona
21. Peralta S, Córdova J, Celis C, Maza D (2020) Numerical modelling of mineral-slurry like flows in a 3D lid-driven cavity using a finite element method based tool. In: ASME international mechanical engineering congress and exposition, vol 84584, p V010T10A023
22. Peralta S, Córdova J, Celis C, Maza D (2022) Parallel domain decomposition of a FEM based tool for mineral-slurry like flows numerical modeling. International Journal of Computational Fluid Dynamics (Under review)
23. Peralta S, Cordova J, Celis C, Maza D (2020) Development of an object-oriented programming tool based on FEM for numerical simulation of mineral-slurry transport. In: International conference on computational science, pp 163–177
24. Altair EDEM, «Altair,» [En línea]. Available: https://www.altair.com/edem/
25. Pöschel T, Schwager T (2005) Computational granular dynamics. Springer, Berlin
26. Kuwabara G, Kono K (1987) Restitution coefficient in a collision between two spheres. Jpn J Appl Phys 26(8R):1230–1233
27. Tsuji Y, Tanaka T, Ishida T (1990) Lagrangian numerical simulation of plug flow of cohesionless particles in a horizontal pipe. Powder Technol 71(3):239–250
28. Zheng Q, Zhu H, Yu A (2012) Finite element analysis of the contact forces between a viscoelastic sphere and rigid plane. Powder Technol 226:130–142
29. Di Renzo A, Di Maio FP (2004) Comparison of contact-force models for the simulation of collisions in DEM-based granular flow codes. Chem Eng Sci 59(3):525–541
30. Langston P, Tüzün U, Heyes D (1994) Continuous potential discrete particle simulations of stress and velocity fields in hopper: transition from fluid to granular flow. Chem Eng Sci 49(8):1259–1275
31. Langston P, Tüzün U, Heyes D (1995) Discrete element simulation of granular flow in 2D and 3D hoppers: dependence of discharge rate and wall stress on particle interactions. Chem Eng Sci 50(6):967–987
32. Norouzi HR, Zarghami R, Sotudeh-Gharebagh R, Mostoufi N (2016) Coupled CFD-DEM modeling: formulation, implementation and application to multiphase flows. Wiley
33. Luding S (2008) Introduction to discrete element methods: basic of contact force models and how to perform the micro-macro transition to continuum theory. Eur J Environ Civ Eng 12(7–8):785–826

34. Maw N, Barber JR, Fawcett JN (1973) The oblique impact of elastic spheres. Wear 38(1):101–114
35. Violeau D (2012) Fluid mechanics and the SPH method: theory and applications. Oxford University Press
36. Cleary PW (2004) Large scale industrial DEM modelling. Eng Comput 21:169–204
37. Ayachit U (2015) The paraview guide: a parallel visualization application. Kitware Inc.
38. Xu Y, Xu C, Zhou Z, Du J, Hu D (2010) 2D DEM simulation of particle mixing in rotating drum: a parametric study. Particuology 8(2):141–149
39. EDEM (2014) EDEM User Guide, Edinburgh: DEM Solutions
40. Li Y, Xu Y, Thornton C (2005) A comparison of discrete element simulations and experiments for 'sandpiles' composed of spherical particles. Powder Technol 160(3):219–228
41. Lorenz A, Tuozzolo C, Louge MY (1997) Measurements of impact properties of small, nearly spherical particles. Exp Mech 37(3):292–298

Publisher's Note Springer Nature remains neutral with regard to jurisdictional claims in published maps and institutional affiliations.

Springer Nature or its licensor (e.g. a society or other partner) holds exclusive rights to this article under a publishing agreement with the author(s) or other rightsholder(s); author self-archiving of the accepted manuscript version of this article is solely governed by the terms of such publishing agreement and applicable law.